Evaluating fluid forces on bluff bodies using partial velocity data

B.T. Tan*, M.C. Thompson, K. Hourigan

Fluids Laboratory for Aeronautical and Industrial Research (FLAIR), Department of Mechanical Engineering, P.O. Box 31, Monash University, Melbourne, 3800, Australia

Abstract

The forces on a bluff body are evaluated by using only velocity information from flow simulations. The "flux" equation formulated by Noca et al. 1999 in 551 is used to achieve this. This only requires time and space derivatives of the velocity field on a surface encompassing the bluff body. This study aims to quantify the accuracy of force predictions when only a subset of the field data is used. Accurate simulations of the two-dimensional (2-D) and three-dimensional (3-D) flow past a circular cylinder provide the time-dependent velocity fields. For purely 2-D flow, the velocity information is limited to a section of the wake and potential flow is assumed on the remaining surface. When the flow is three dimensional, it is assumed that only a 2-D projection of the velocity field on a single plane is known (as is often the case with experimental PIV measurements). Statistical quantities of the lift and drag forces from these predictions are compared to the forces obtained by directly integrating the pressure and shear stress over the body surface. The relative phasing between the two signals is also presented in the 2-D flow case. In the 3-D flow case, predictions from numerous planes are averaged in an attempt to improve the overall force estimate. The results show that some quantities can be accurately predicted, such as the phasing of the lift and drag forces in the 2-D simulations, and the mean drag force and the fluctuating lift force for the 3-D flows. Predictions are generally better when the integration boundary is closer to the cylinder. Importantly, this study provides an indication of the maximum accuracy achievable using restricted experimentally derived velocity fields to compute forces experienced by bluff bodies.
© 2004 Elsevier Ltd. All rights reserved.

1. Introduction

Over the years, marked improvements have been made in experimental techniques to extract velocity fields in two-dimensional (2-D) planes (e.g., Adrian, 1991; Upatnieks et al., 2002), or even three-dimensional (3-D) volumes (e.g., Konrath et al., 2002; Hinsch, 2002). For 2-D fields using particle image velocimetry (PIV), this is due to a combination of factors including the increase in capacity and speed of charge-coupled devices, more-powerful and less-expensive compact lasers, availability of cheaper large fast memory and hard-disk storage, and refinement of analysis techniques and software. Coupled together, these improvements allow high-density accurate 2-D velocity field projections to be extracted rapidly in 2-D planes (Upatnieks et al., 2002). Augmented with multiplane or laser sheet scanning techniques

---

*Corresponding author.

  E-mail address: kenny.tan@eng.monash.edu.au (B.T. Tan).

(Scarano et al., 2002; Heineck et al., 2002; Etoh et al., 2002) and stereoscopic systems (e.g., Meyer et al., 2002), such experimental techniques can provide a substantial velocity field map over a domain of interest.

For wake studies, this increase in the capability of obtaining accurate experimental velocity data has led to the question of whether these fields can be used solely to determine accurate fluid forces acting on the bluff body generating the wake (e.g., Lin and Rockwell, 1996; Unal et al., 1997). While sometimes this can be done directly using a force balance, for other situations it may be difficult, complex or expensive to do. However, knowledge of the fluid forces acting on a body is vital in the important area of fluid–structure interaction, with wide applications to economically significant industries such as aeronautics/aerospace, offshore marine hydrodynamics and building aerodynamics.

Often PIV data is available only over a small window which does not encompass the whole wake and may or may not include the bluff body. Even if the body is included in the analysis window, the extracted velocity field near the surface is usually far from accurate or reliable because of various factors including the difficulty of seeding the flow in this region, difficulties in lighting (because of the shadow cast by the body) and the limited dynamic range of PIV which means low velocities are difficult to determine. Thus, it is usually not possible to determine the velocity field near the body directly.

Noca et al. (1999) derived several integral methods to calculate the fluid forces acting on a body without any direct pressure information. These include two methods that require integration of velocity data over an area (in two dimensions) or a volume (for three dimensions) enclosing the body, and a method that reduces these integrals to be over the bounding lines 2-D or surfaces 3-D. This latter approach, using the "flux equation", appears particularly attractive since limited (time and space-varying) velocity data over just a closed curve (or surface) encompassing the body should allow the forces to be determined. Noca et al. (1999) demonstrated the feasibility and accuracy of the method by using both experimental and numerical velocity fields to reconstruct the lift and drag on a cylinder. This builds on an earlier study by Unal et al. (1997).

The main aim of this article is to examine if accurate force predictions can be obtained with just a limited subset of the entire velocity field. In particular, this study aims to provide some answers the following two questions. (i) For purely 2-D flows, how accurately can the fluid forces acting on the body be evaluated when only the velocity components and their derivatives along a line through the wake are known? (ii) For 3-D flows, how large are the errors caused by using a 2-D slice of the velocity field and its in-plane derivatives to estimate the lift and drag forces experienced by an object? For the latter question, no information about the out-of-plane component of velocity and spatial derivatives in the out-of-plane direction are used. Therefore, only the out-of-plane component of vorticity can be evaluated. The field will not be divergence-free without the out-of-plane velocity information. This is typical of data obtained by conventional PIV systems and hence is the focus of the 3-D study.

The flow around a 2-D circular cylinder is chosen for this investigation. This geometry is used because it has been well studied and provides a simple geometry with only one length scale. Therefore, the only dimensionless parameter governing the flow is the Reynolds number (Re). As the Reynolds number is increased, the flow undergoes transition from steady attached flow to 2-D Karman vortex shedding. Further increases result in the development of spanwise instabilities which distort the 2-D shedding. Two-dimensional von-Karman vortex shedding develops above the Hopf bifurcation at $\mathrm{Re}_{C1} \approx 46$ (Dusek et al., 1994). Theoretical predictions using Floquet analysis show that the first transition to 3-D flow occurs at $\mathrm{Re}_{C2} \approx 189$ (Barkley and Henderson, 1996). This flow state, commonly referred to as *Mode A*, has a spanwise wavelength of $\lambda_z = 3.96d$, where d is the cylinder diameter. The next transition to *Mode B* shedding is predicted from linear analysis to occur at $\mathrm{Re} \approx 259$. This secondary instability has a spanwise wavelength of $\lambda_z \approx 0.88d$ (Barkley and Henderson, 1996), and the remnants of this mode persist well into the fully turbulent regime (Wu et al., 1996). In practice, Mode B comes in at lower Reynolds numbers ($\mathrm{Re} \gtrsim 230$); the discrepancy occurs because the analysis assumes a 2-D base flow. Experiments by Williamson (1988) and computations by Henderson (1997) observed a sudden drop in mean drag force associated with the onset of Mode A shedding and a recovery in drag force with the transition to Mode B. This has been associated with a drop in spanwise correlation associated with the first transition followed by a partial recovery at the next transition.

In this article, flow simulations and analysis are presented for two Reynolds numbers. The first is $\mathrm{Re} = 150$, where the flow is purely two dimensional. This allows predictions to be analysed first in the less complex 2-D case. The second Reynolds number chosen was $\mathrm{Re} = 260$, and the flow is accurately simulated using a fully 3-D code. This is high enough to allow both 3-D instability modes to exist. Indeed simulations show there is competition between the modes; over some time intervals Mode A is clearly dominant while at other times Mode B is the preferred mode.

The organization of the paper is as follows. The next section outlines the methodology used in this study. This includes a description of the numerical techniques and parameters used to simulate the flow. Following this, the details of the integration boundaries, and the technique used to calculate the force components from the velocity information provided by the flow simulation are given. The results section compares the predictions of drag and lift forces for both the two- and 3-D flows, followed by a discussion of these results. Finally, the conclusions from this study are presented.

2. Methodology

Figs. 1 and 2 show the problem setup for this study. For convenience, the freestream velocity vector has a magnitude of one unit and the direction is from left to right in these figures. The diameter of the cylinder, d, is the characteristic length scale used for evaluating Re. The computational domain in 3-D simulations has a spanwise length of λ and periodicity is imposed at the cylinder ends. This is indicated by the larger grey circles at the ends of the cylinder in Fig. 2. All values for D in this study is relative to the diameter of the cylinder, d.

2.1. Flow simulation

The flow simulated is governed by the time-dependent incompressible Navier–Stokes equations. Spatial discretization is achieved using the spectral/spectral-element method (Karniadakis, 1990) and the equation system in integrated forward in time using a classical three-step time-splitting technique [e.g., Karniadakis et al., 1991]. The spectral-element method is essentially a modified Galerkin finite-element method which incorporates a tensor-product polynomial expansion within each macro-element. In this study, 11th order polynomials are used internally. Global Fourier expansions are used for the spatial discretization of flow variables in the spanwise direction, which results in a periodic boundary condition at the ends of the span as indicated previously. The overall scheme is second-order accurate in time through incorporating high-order pressure boundary conditions as described in Karniadakis et al. (1991). This technique (and the associated software) has been used in many previous studies to accurately simulate flow around a bluff bodies [e.g., Thompson et al., 1996; Tan et al., 1998; Hourigan et al., 2001].

Fig. 3 shows a 2-D slice of the computational mesh used for all the simulations. This plot shows only the macro-elements. Each element consists of a further 12×12 internal nodes. To the front, top and bottom of the cylinder, the computational grids extends $6d$ and employs Chebyshev (cosine) stretching. Seven elements are used to span the gap
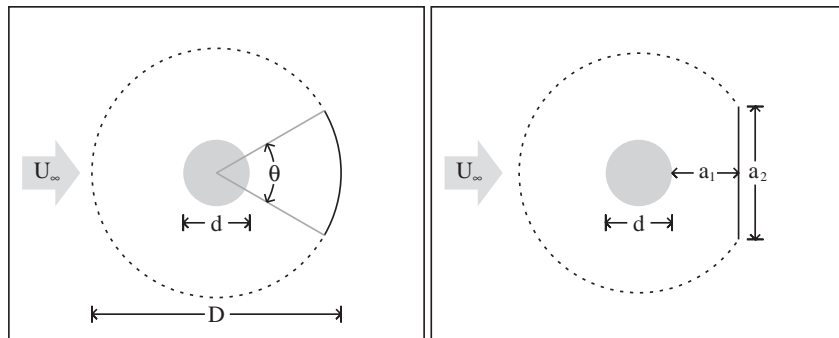

Fig. 1. Schematics showing the circular cylinder and the integration boundaries for force predictions associated with the 2-D flow. Actual velocity data from the simulations are used over the solid arc (left) or line (right) and the velocity field from the potential flow solution is used over the dashed portion.
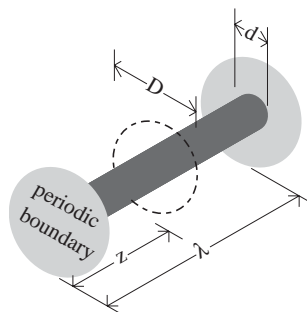

Fig. 2. A sketch of the circular cylinder and the dimensions involved in the 3-D simulations.
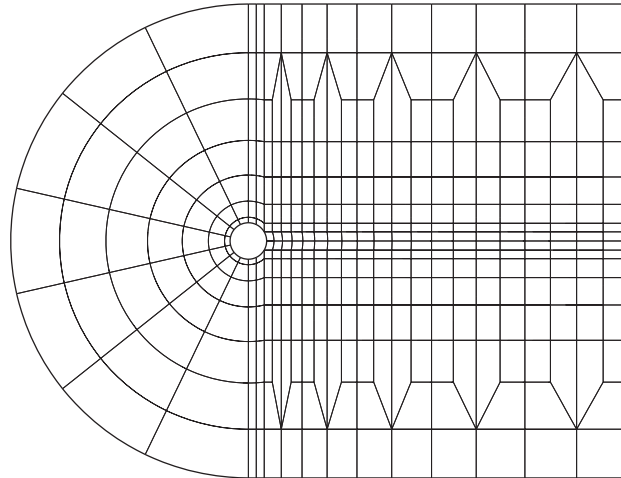
Fig. 3. A plot of the computational grid showing only the macro elements.

with an initial size of $0.15d$. Downstream of the cylinder, a less severe hyperbolic tan stretching is used to span $10d$ with twenty elements and an initial size of $0.27d$. The length of the elements on the cylinder surface are $0.22d$ on the leading face and $0.27d$ on the trailing face.

The boundaries on the top, upstream and bottom of the cylinder are all set to the free-stream velocity. Zero normal velocity gradients are set on the outflow boundary. The time-step used in these simulations was $\delta t = 0.002d/U_\infty$ relative to a flow period of approximately $T = 5.15$ when Re = 150 and $T = 4.7$ when Re = 260. A very conservative time-step was employed to meet the stability criteria resulting from the high spatial resolution and the explicit nature of the convective substep of the scheme. Besides the high resolution near the cylinder, the grid is stretched only gradually away from the body surface so that good resolution is still available at the outer surfaces used for integration to estimate the force.

In the first part of this study, focusing on 2-D flow, simulations were performed at Re = 150. The simulations were impulsively started and analysis was only undertaken once the drag and lift trace showed periodicity. No perturbation was introduced to instigate the shedding. Subsequently, the 3-D simulations were performed at Re = 260. Initially, a 2-D simulation was evolved until it reached a periodic state. This solution was then mirrored across the span. At the start of the 3-D simulation, a white noise perturbation of relative magnitude 10^{-3} was added to all components of the flow velocity at each node.

This latter half of this study is mainly concerned with force prediction from strongly 3-D flows. A spanwise domain of $\lambda = 3.96d$ was chosen for this study. Only wavelengths that are integer divisible into λ can exist in this domain. This captures either one wavelength of Mode A shedding ($3.96d$) or 4 wavelengths of Mode B shedding ($0.99d$). Although these are close to the theoretical estimates of the preferred wavelengths at onset, they are artificially imposed by the selection of the spanwise domain size. A much larger spanwise domain capturing several modes is required for accurate predictions of post-transition flow quantities (Henderson, 1997). However, this minimal spanwise domain is sufficient for this study as it produces 3-D flows with the consistent vortical structures associated with Mode A and Mode B shedding.

The drag and lift forces on the cylinder are calculated directly from the flow simulation by integrating the pressure and viscous stresses around the cylinder. To maintain a high order of accuracy, the stresses and the integrals which determine the body force components are calculated with the same spatial discretization scheme as the flow and the integration is performed using the same quadrature as for the spectral and spectral-element schemes.

2.2. Force calculation

2.2.1. Two-dimensional flow

This section outlines the method used to estimate the force when flow information is only available on a single plane. This includes the 2-D flow cases and the situation where only a single plane of flow data is available when the flow is three dimensional. The "flux equation" as described by Noca et al. (1999) is used to evaluate the force (**F**) on the

cylinder. This equation in vector form is reproduced here in Eqs. (1) and (2) as follows:

$$\mathbf{F} = \oint_{S(t)} \hat{\mathbf{n}} \cdot \gamma_{\text{flux}} \, \mathrm{d}S - \oint_{S_b(t)} \hat{\mathbf{n}} \cdot (\mathbf{u} - \mathbf{u}_s) \mathbf{u} \, \mathrm{d}S - \frac{\mathrm{d}}{\mathrm{d}t} \oint_{S_b(t)} \hat{\mathbf{n}} \cdot (\mathbf{u}\mathbf{x}) \, \mathrm{d}S, \tag{1}$$

where

$$\gamma_{\text{flux}} = \frac{1}{2} \mathbf{u}^2 \mathbf{I} - \mathbf{u}\mathbf{u} - \frac{1}{N-1} \mathbf{u}(\mathbf{x} \wedge \boldsymbol{\omega}) + \frac{1}{N-1} \boldsymbol{\omega}(\mathbf{x} \wedge \mathbf{u}) - \frac{1}{N-1} \left[\left(\mathbf{x} \cdot \frac{\partial \mathbf{u}}{\partial t} \right) \mathbf{I} - \mathbf{x} \frac{\partial \mathbf{u}}{\partial t} + (N-1) \frac{\partial \mathbf{u}}{\partial t} \mathbf{x} \right]$$
$$+ \frac{1}{N-1} [\mathbf{x} \cdot (\nabla \cdot \mathbf{T}) \mathbf{I} - \mathbf{x}(\nabla \cdot \mathbf{T})] + \mathbf{T}. \tag{2}$$

Here, $\mathbf{u}$ and $\boldsymbol{\omega}$ are the velocity and vorticity vectors, respectively. Also, $S(t)$ is an arbitrary closed surface (line in 2-D) encompassing the entire body while $S_b(t)$ is the closed surface (line) of the body. Although these surfaces (lines) can be time-dependent, they are stationary in this study. The normal unit vector to these surfaces (line) is $\hat{\mathbf{n}}$. The parameter N is the number of spatial dimensions (i.e. $N = 2$ for 2-D and $N = 3$ for 3-D). The other terms are: $\mathbf{u}_s$, the body wall velocity, $\mathbf{T}$, the viscous stress tensor, $\mathbf{I}$, the unit tensor, and $\mathbf{x}$, the position vector from an arbitrary location. In this study $\mathbf{x}$ is measured from the centre of the cylinder. The second and third term on the right-hand side of Eq. (1) have no contribution in this case because the cylinder is stationary with no flow through the surface (line).

The vector force calculated from Eq. (1) is exact when the velocity field is divergence-free (i.e., for incompressible flow) and satisfies the momentum equations. The derivation and proof are given in Noca et al. (1999). As can be seen, no pressure information is required to calculate the force on the body. Another advantage of this formulation is that information is only required on two closed surfaces (lines). The first being the boundary of the body itself and the second is an arbitrary surface (line) encompassing the body. This arbitrariness allows exclusion of regions where data is less accurate.

In the 2-D cases, two different shapes are used for the outer perimeter as shown in Fig. 1. The first shape is a circular ring centred at the origin of the cylinder with a diameter D. The second shape consists of a line normal to the flow and across the wake. This line is placed at a distance a_1 downstream of the cylinder and has a length of a_2. The perimeter is closed with a circular arc, which is also centred at the origin of the cylinder. A concentric circular ring of diameter D is also used in the 3-D case as shown in Fig. 2. When a 2-D slice is used to predict the force in the 3-D flow, it is positioned at coordinate z from the periodic boundary. On this slice, the out-of-plane component of velocity is not used and parameter N is set to 2.

The velocity gradients appearing in the integrand in Eq. (1) are evaluated using polynomial interpolation consistent with the spectral-element expansion. The flow variables are interpolated to 6000 equispaced points on the circular ring defining the outer boundary. When two line segments are used in the 2-D case, each segment also consists of 6000 equispaced points. The number of equispaced points on the ring is in excess of the spatial resolution used for flow simulation. Integration is then performed using Simpson's $\frac{3}{8}$th rule. Time derivatives are also required. A centered-difference stencil is used to evaluate these terms consistent with the accuracy of the time-stepping method employed for the flow computations. Recall that a very small time-step is used.

2.2.2. Three-dimensional flow

An outer surface that fully encompasses the body is required in order to use the "flux equation" as shown by Eqs. (1) and (2). It is impossible to obtain an outer surface that fully encompasses the cylinder in a periodic domain. The cylinder will always protrude out of the integration surface at the periodic boundaries. This outer surface therefore will always have two circular holes. Consequently, the "flux equation" of Noca et al. (1999) needed to be modified for this particular problem. The modified equation is as follows:

$$\mathbf{F} = \int_{S(t)} \hat{\mathbf{n}} \cdot \gamma_{\text{flux}} \, \mathrm{d}S - \int_{S_b(t)} \hat{\mathbf{n}} \cdot (\mathbf{u} - \mathbf{u}_s) \mathbf{u} \, \mathrm{d}S - \frac{\mathrm{d}}{\mathrm{d}t} \int_{S_b(t)} \hat{\mathbf{n}} \cdot (\mathbf{u}\mathbf{x}) \, \mathrm{d}S, \tag{3}$$

where

$$\gamma_{\text{flux}} = -\mathbf{u}\mathbf{u} - \frac{\partial \mathbf{u}}{\partial t} \mathbf{x} + \mathbf{T} + \left[\int_{\mathbf{x_o}}^{\mathbf{x}} \hat{I} \cdot \left(\frac{\partial \mathbf{u}}{\partial t} + \mathbf{u} \cdot \nabla \mathbf{u} - \nabla \mathbf{T} \right) \mathrm{d}l \right] \mathbf{I} \tag{4}$$

and $\hat{I}$ is the unit tangential vector. An outline of the required modification is included in the Appendix.

The chosen outer surface consists of a concentric circular tube of diameter D spanning the entire domain and circular disks at the periodic boundaries. The solid cylinder protrudes out of the end circular disk. The contribution from these end disks to the spanwise force cancel when identical surfaces are used on both ends and therefore these term can be

ignored in this case. The surface integration is performed by firstly interpolating the velocity field to 6000 equispaced points on the outer circular boundary on each Fourier plane. The field is then transformed to Fourier space where the integration in the spanwise direction is trivial. Finally, integration around the circular line on a plane is done using Simpson's $\frac{3}{8}$th rule. For the double quadrature, the starting point is chosen to be an arbitrary point on the circular tube at the periodic boundary. Integration is first performed between points around the tube on that plane (using ninth-order Gaussian quadrature) thus forming a circle. Each of these points then becomes the basis for integration in the spanwise direction using Fourier expansion.

3. Results and discussion

3.1. Flow simulation

3.1.1. Two-dimensional flow

The 2-D flow is simulated at Re = 150 for 200 time units from an impulsive start to allow for the decay of any transients. The ensuing traces of lift and drag forces are periodic, as shown in Fig. 5. Fig. 4(a) shows a contour plot of vorticity when the lift force is maximal. The dark and light colouring represents positive and negative vorticity, respectively.

A previous study by Henderson (1997) has shown that blockage in the 2-D plane can affect the prediction of surface pressure and therefore the resulting force for flow past a circular cylinder. For both two- and 3-D simulations in this study, the placement of the boundaries are a compromise between minimizing blockage and the computational cost of devoting more resolution to regions nearer the cylinder. However, any blockage effects will affect both the force predicted directly by the simulation and that from evaluating the flux integral. Therefore, blockage effects are of less importance in this study.
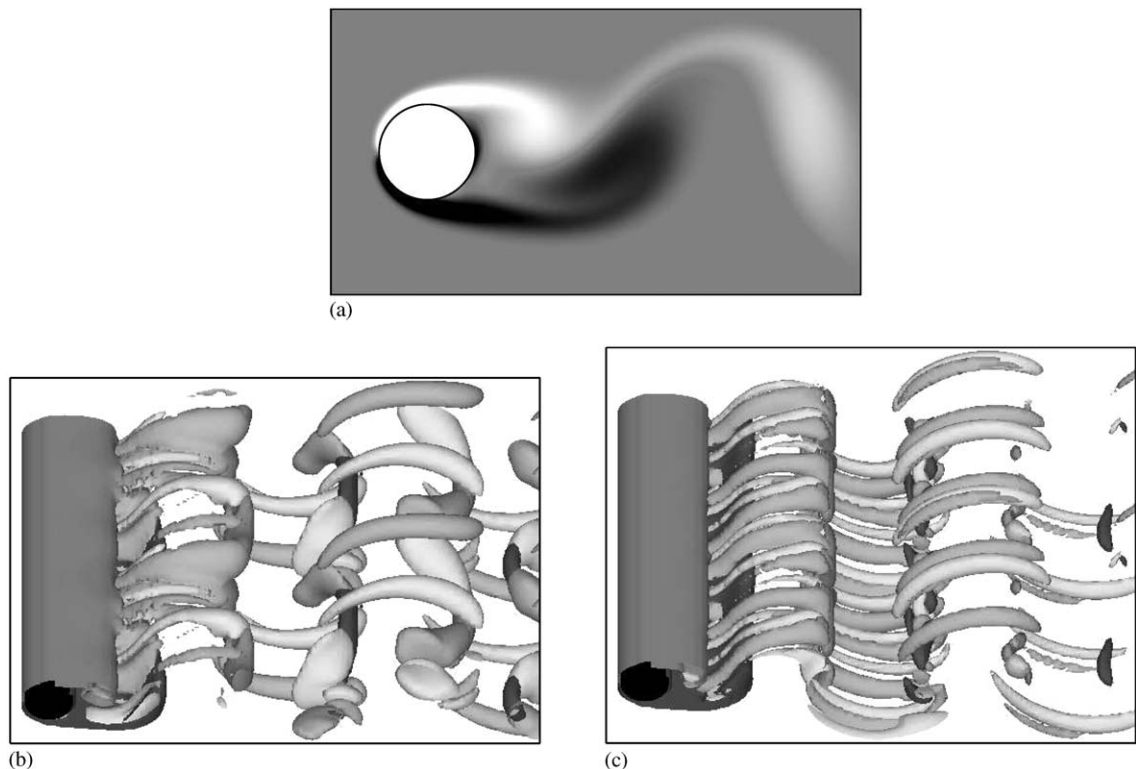

(a)

(b)

(c)

Fig. 4. (a) Greyscale vorticity plot showing characteristic wake vortices for Re = 150; (b), (c) iso-surfaces of positive and negative spanwise and streamwise vorticity for Re = 260. Middle plot corresponds to a time when the wake is predominately shedding Mode A structures. Bottom plot corresponds to a time when Mode B is more dominant.

3.1.2. Three-dimensional flow

The 3-D instability required many shedding periods to saturate from a slow initial growth. Flow visualizations show that Mode A shedding dominated between $t = 130–150d/U_\infty$ (approximately 25–30 shedding cycles) measured from the start of the 3-D simulation. Mode A shedding gradually loses its dominance and Mode B develops as the flow evolves. Visualizations show that Mode B is the dominant shedding mode between $t = 180–200d/U_\infty$. When the flow is simulated further, it switches between these shedding modes and, at times, even shows predominately 2-D shedding. This behaviour has been observed previously in similar numerical simulations (Thompson et al., 1996), and it was a conscious choice to select a Reynolds number that led to this mode switching. Williamson (1988, 1996) experimentally found that for slightly higher Reynolds numbers, Mode B dominates and thus leads to a more regular wake. At higher Reynolds numbers still, at least up to Re = 1000, the remnants of Mode B persist (Wu et al., 1996) and hence the results of this investigation have relevance to significantly higher Reynolds number flows. A result of this mode-switching is that the flow is only dominated by one shedding mode for a few shedding cycles. In this study, five shedding cycles are chosen as representative of each shedding mode. Whilst in general, such a short time series may be inadequate for obtaining statistically accurate quantities, in this case however, the shedding is almost repeatable, as can be seen in the drag and lift traces obtained directly from the simulations in Figs. 15 and 16. Therefore, this sampling time should be adequate to provide a indicative comparison of the mean and standard deviation of force coefficient predictions.

The iso-surface plots shown in Fig. 4(a) and (b) correspond to when the flow is predominantly Mode A and Mode B, respectively. The cylinder is coloured black, the two darker shades are iso-surfaces of spanwise vorticity with a strength $\pm 3.0 U_\infty/d$ and the two lighter shades are iso-surfaces of streamwise vorticity at $\pm 1.0 U_\infty/d$. For clearer visualizations, Fig. 4(b) and (c) show twice the actual computational domain in the spanwise direction.

Of relevance to the application of the findings of this study, the following points are noted. Mode A shedding is associated with significant distortion of the Karman vortex rollers as can be observed from the plots in Fig. 4(b). Thus, there are likely to be significant variations in the local force coefficients across the span. In contrast, Mode B shedding has a significantly smaller distorting effect on the Karman vortex rollers, which again can be seen from the flow visualization in Fig. 4(c). At higher Reynolds numbers, Mode B is the dominant mode. In experiments of flows past long cylinders, depending on the end conditions, oblique shedding is often observed (Williamson and Roshko, 1988; Albarede and Provansal, 1995). This means that there will be a shift in the mean phasing of shedding depending on the position along the span. Finally, another important phenomenon observed in cylinder wake flows is that of *dislocations* (Williamson, 1996), in which shedding from one section of the cylinder becomes dislocated from a neighbouring part. It is envisaged that dislocations will lead to significant changes in the local force coefficients measured at the cylinder surface.

3.2. Force prediction

The numerical approach of predicting the fluid forces via the flux equation can be tested by comparing them with those obtained directly from the numerical simulation. Both predictions should match when $\theta = 360°$ in the 2-D flow (see Fig. 1) and when the outer surface encompasses the entire cylinder in the 3-D simulation (except for the protrusion on the periodic boundary). Tests were performed for both two- and 3-D flow conditions. The integration boundary, D, was varied between 2.0–6.0 and 1.5–3.0 in the two- and 3-D flow cases, respectively. Figs. 5, 13 and 14 shows a sample of drag and lift coefficient traces for 2-D, Mode A and Mode B shedding. For each case, and all values of D, the forces predicted by integration and directly from the simulation were compared over a long period (over $300d/U_\infty$ sampled at $0.2d/U_\infty$). The deviation in drag coefficient relative to the mean and the lift coefficient relative to the peak-to-trough never exceed 4% at any time. This supports the studies of Noca et al. (1999) and helps to validate the implementation of this somewhat complex method.

3.2.1. Two-dimensional flow

Fig. 1 shows the integration boundaries used to predict the forces. Flow data from the simulations are used on only a limited section of this boundary that intersects the wake. This is either: (i) an arc, which is part of a circle with a diameter of D spanning an angle of θ about the centreline of the cylinder; or (ii) a line normal to the free stream with length a_2 and a downstream distance of a_1 to the cylinder. Over the remainder of the boundary, the flow is assumed to be steady potential flow. For the force prediction using the circular arc, D varied between 2.0 and 6.0d in increments of d, with θ between 60° and 180° in increments of 30°. In the case with the straight line, a_1 varied between 0.5d and 2.5d in increments of 0.5d and a_2 varied between 1.0 and 5.0 in increments of d.

Figs. 6 and 7 shows a selection of cases where flow velocity data is used on only a limited section of the integration path. Most cases show approximately a sinusoidal trace. The exceptions are when the arc is small or the line is short,
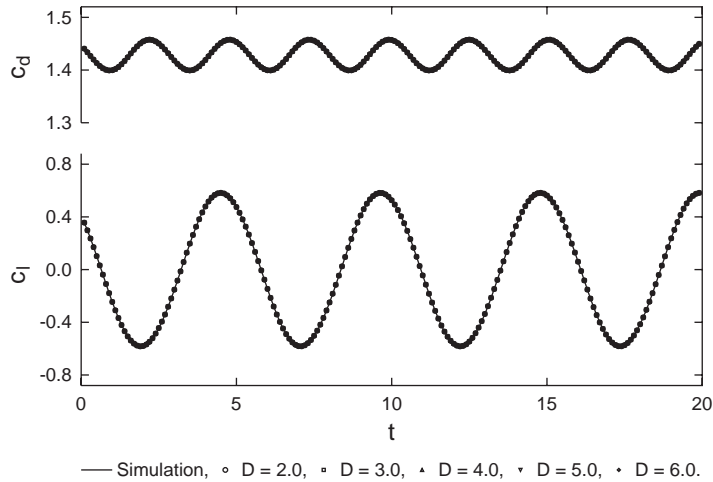
Fig. 5. The drag and lift forces predicted by the simulation compared with those from line integration when the 2-D flow is at Re = 150. The line integration is performed for various values of D, with $\theta = 360°$.

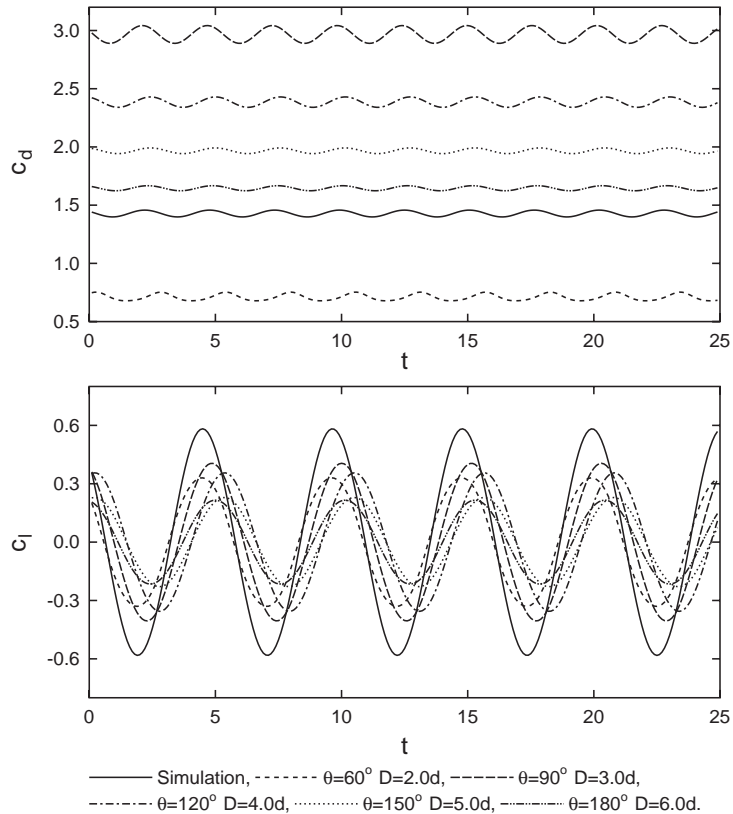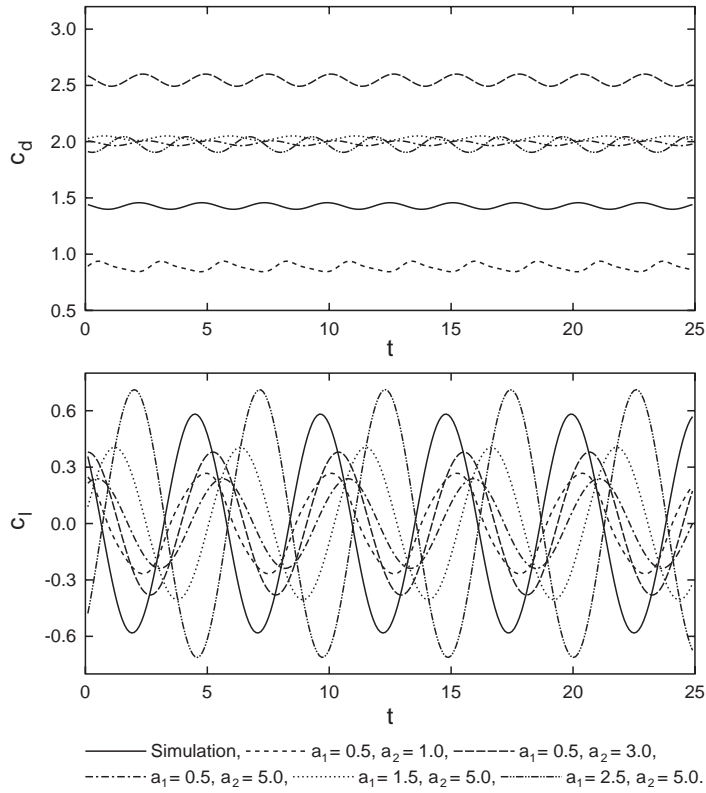Fig. 6. A selection of time histories of drag and lift coefficients for 2-D flow at Re = 150, corresponding to arcs of different angles and radii.

and placed near the cylinder for the drag force prediction. For a more detailed statistical analysis, data were sampled at intervals of 0.1 time units for approximately 50 time units (i.e., 10 complete shedding cycles).

Figs. 8 and 9 are plots of mean and standard deviations of the drag coefficient. Fig. 10 shows the standard deviations of the lift coefficient. The phase of the drag and lift traces relative to the traces obtained from the simulation are plotted

Fig. 7. A selection of time histories of drag and lift coefficients for 2-D flow at Re = 150, corresponding to various lines across the wake, a_1 and a_2.
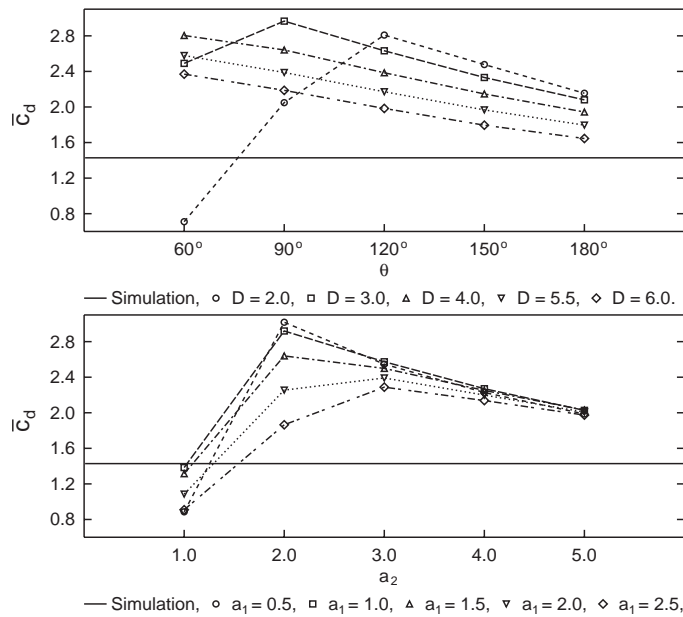
Fig. 8. Mean drag coefficient predictions as a function of (i) θ and D (top), and (ii) a_2 and a_1 (bottom), compared with the simulation (solid line).
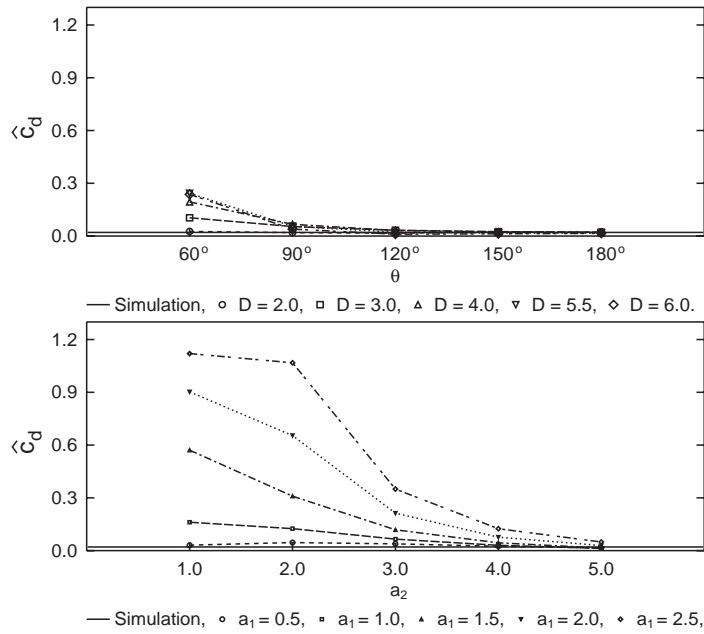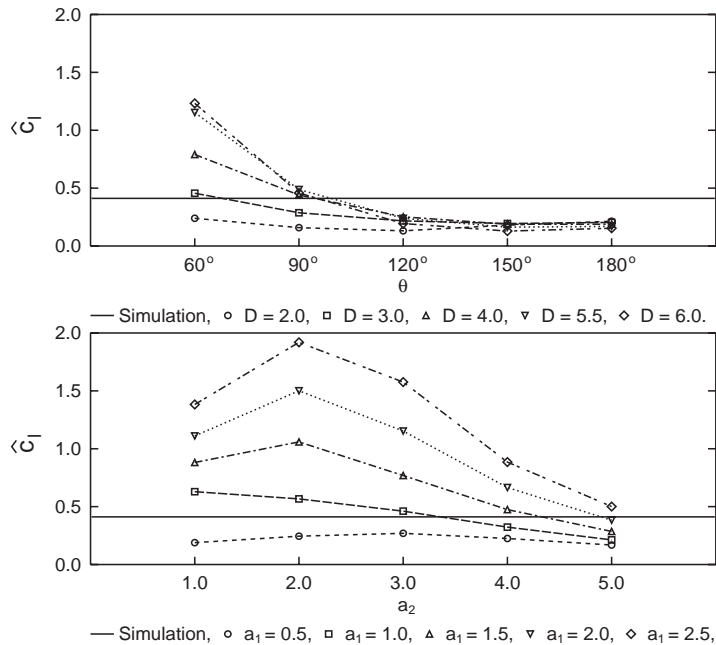
Fig. 9. Standard deviation of drag coefficient predictions as a function of (i) θ and D (top), and (ii) a_2 and a_1 (bottom) compared with the simulation (solid line).

Fig. 10. Standard deviation of lift coefficient predictions as a function of (i) θ and D (top), and (ii) a_2 and a_1 (bottom) compared with the simulation (solid line).

in Figs. 11 and 12, respectively. All these graphs are plotted as a function of D for various θ, or of a_2 for various a_1. The mean drag and standard deviations obtained directly from the flow simulation are plotted with a solid line. The predictions have no mean lift because the integration boundaries are symmetric about the centreline. The shedding period in this case was 5.15 time units. The lift signal oscillates with this period and the drag signal oscillates at half this
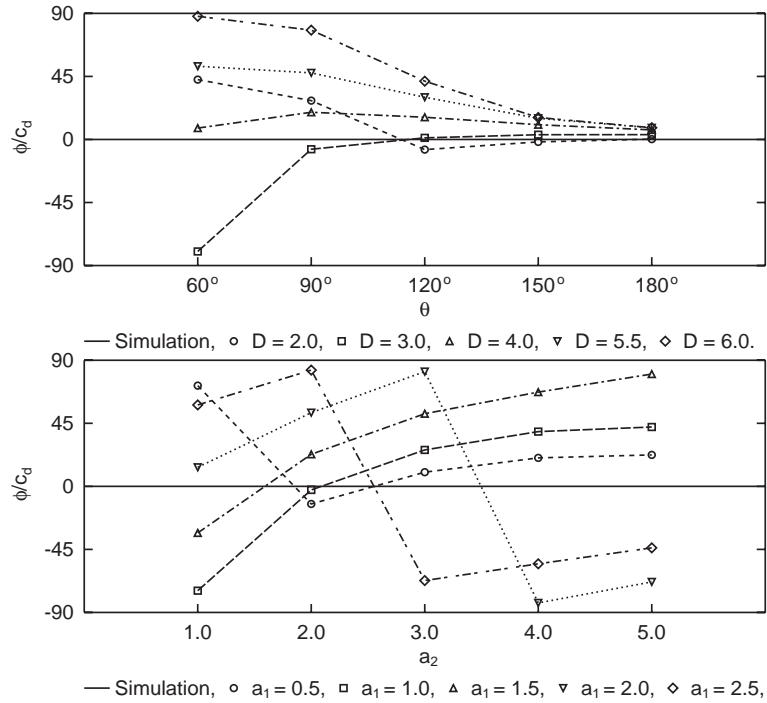
Fig. 11. The phase difference in drag time traces between the prediction and the simulation, for predictions with various (i) θ and D (top), and (ii) a_2 and a_1 (bottom).
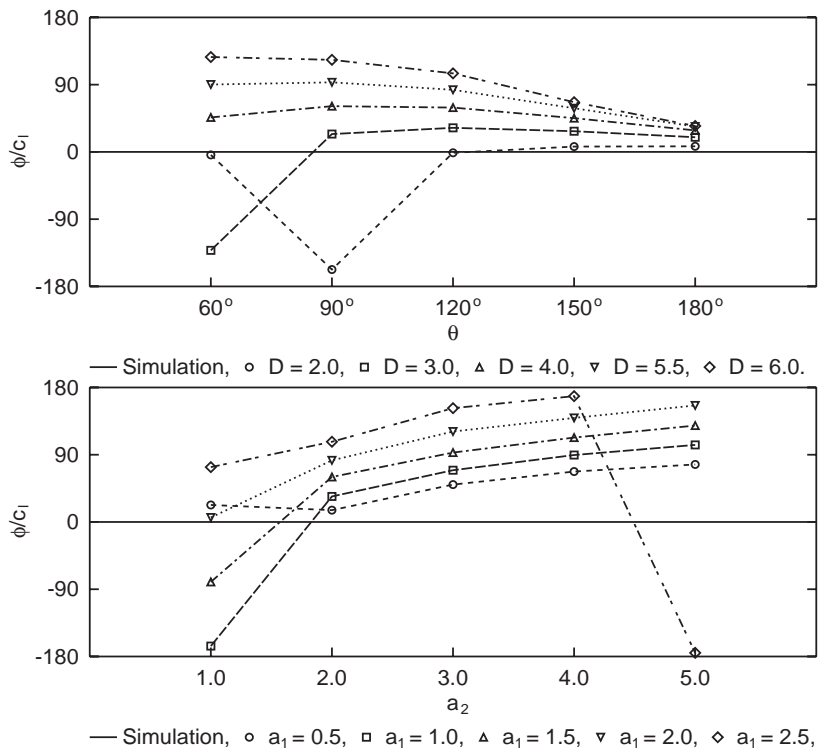

Fig. 12. The phase difference in lift time traces between the prediction and the simulation, for predictions with various (i) θ and D (top), and (ii) a_2 and a_1 (bottom).

period due to the wake symmetries involved. The phase difference in the plots is measured by comparing the time difference between the peaks in the predicted force and the direct simulation relative to the flow period. A positive difference means the trace from the prediction leads that of the simulation.

The primary aim here is to study the viability of predicting the fluid forces on the bluff body with these limited data. The reasons the two predictions differ in this exercise can be summarized through the following points. The fluctuations in the wake region are large relative to other regions of the flow. Although this implies that predictions should include the bulk of the fluctuating components, the fluctuations in the remainder of the flow, although locally small, may not sum to be insignificant. The other source of error can be attributed to the differences between the mean flow and the potential flow. It was expected that the upstream flow should be a reasonable model as well as the flow at the sides far from the body. However, in the case studied here, the Reynolds number is low and hence the influence of the body extends much further than it does at higher Reynolds numbers.

There are several common characteristics shown by the statistical quantities of drag and lift forces presented in Figs. 8–12. Obviously, the prediction improves when a larger portion of the wake is used (i.e. larger values of θ or a_2). The predictions also improve when the integration perimeter is nearer the cylinder (i.e. smaller values of D or a_1), except for mean drag where the opposite is true. Fig. 8 shows that better predictions are obtained when the boundary is placed further away (i.e. larger values of D or a_1), presumably because the flow approaches the potential flow. The convergence is slow and the best prediction in this study (i.e. $D = 6.0$ and $\theta = 180°$) is only accurate to within about 10%. For the cases presented, predictions that use a circular arc with larger values of θ are better than those than those obtained with a straight line across the wake. This is the result of using a larger portion of the real flow data over the potential flow data.

The standard deviation and phase error for both lift and drag forces improve when obtained using integration boundaries closer to the cylinder (i.e. smaller values of D or a_1). This is clearly evident in the standard deviation of the drag coefficient shown in Fig. 9. The standard deviation of the lift coefficient in Fig. 10 converges to a value that is different to that simulated, implying that the front half of the flow has a significant contribution. In hindsight, this behaviour is perhaps less surprising, given the lift force will be more influenced by the fluctuating flow at the sides of the cylinder, while the drag is affected by the fluctuations mainly at the rear. Hence, good lift predictions, and predictions of the standard deviation of drag force, probably require data covering $\theta > 180°$. The phase difference in Figs. 11 and 12 show good convergence for larger values of θ when an arc is used. When a straight line is used, convergence may still be possible for larger values of a_2 than considered here. It is expected that predictions overall will improve as the Reynolds number is increased since the potential flow approximation away from the body will become increasingly accurate, although as we will see, the onset of 3-D flow introduces new difficulties.

3.2.2. Three-dimensional flow

Figs. 13 and 14 show that an accurate prediction of the forces acting on the cylinder can be obtained when the 3-D flow field information is integrated over the surface encompassing the cylinder.

Next, the force is predicted by using only 2-D velocity information on a slice through the 3-D flow. As described previously, the out-of-plane component of velocity is discarded for the purpose of this exercise, as this information is generally not available from standard PIV techniques. The force predicted directly from the flow simulation is a spanwise-averaged force. Fig. 2 shows the integration boundary. Again, the integration boundary is a circle of diameter D centered at the centre of the cylinder. The circle is on a plane parallel to the periodic boundaries and at distance of z from one of them. For this set of results, the velocity field over the entire integration contour is used to estimate the force. The consideration of two different shedding modes provides an indication of the sensitivity of the predictions, especially since Mode A leads to large distortions to the Karman vortices and Mode B much less so.

The force is predicted using integration contours with radii between $D = 1.5$–$3.0d$ in intervals of $0.5d$. The plane is placed at 32 equispaced locations across the span. The velocity field is sampled every 0.2 time units, corresponding to approximately 24 points per cycle. Statistics are collected over approximately 20 time units for each shedding mode. Figs. 15 and 16 show selected temporal traces of the force components predicted using the analysis and directly from the flow simulation. For both shedding modes the mean drag coefficient is predicted reasonably well, but not the fluctuating component, especially when the integration boundary is placed further from the cylinder. The lift force traces shows good agreement for the mean and fluctuating components as well as the phasing.

The predicted mean drag and lift coefficient are plotted as z is varied across the span for the various value of D in Figs. 17 and 18, for both Mode A and Mode B shedding. The standard deviation of the drag and lift coefficient is plotted in Figs. 19 and 20. Care is taken to ensure that entire flow periods are considered for statistical analysis.

In an attempt to obtain a better estimate that is less dependent on z, n individual planes are averaged. These planes are chosen to be equispaced across the span. The mean drag and lift coefficient are plotted in Figs. 21 and 22. The standard deviation of drag and lift coefficient are plotted in Figs. 23 and 24.
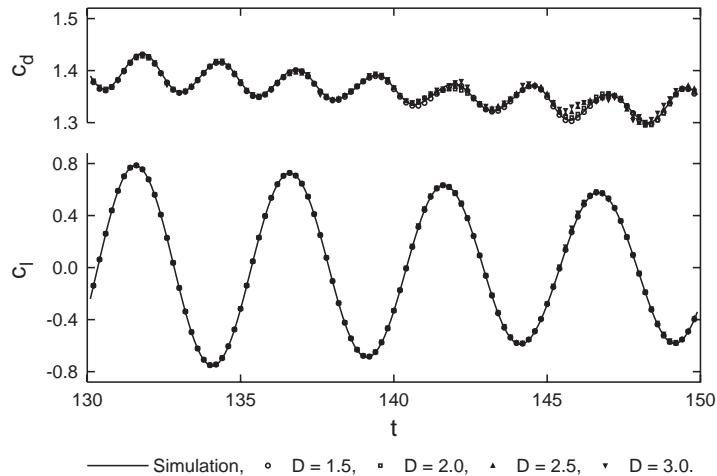
Fig. 13. Comparison of drag and lift coefficients calculated both from surface integration and from direct simulation for Mode A shedding at Re = 260.
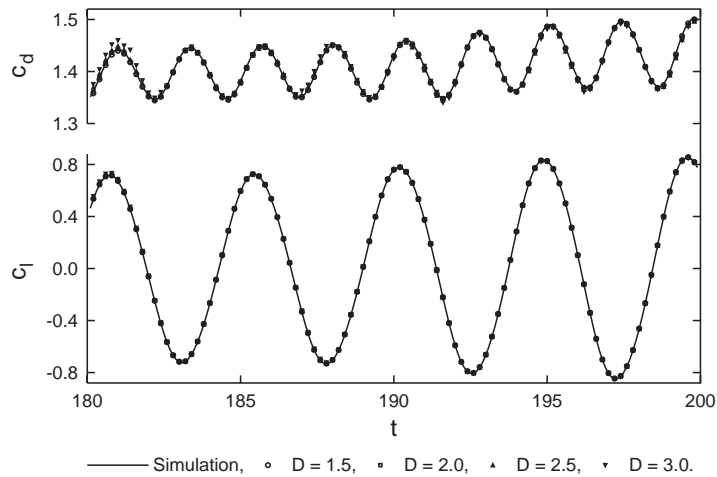

Fig. 14. Comparison of drag and lift coefficient calculated both from surface integration and from direct simulation for Mode B shedding at Re = 260.

The predictions are generally better when a smaller integration perimeter is used (D). The mean drag coefficient in Fig. 17, and the standard deviation of the lift coefficient in Fig. 20, show similar trends. The Mode A shedding in both cases shows a spanwise wavelength equivalent to the spanwise domain size of the flow. The magnitude of the spanwise variation increases with the size of the integration boundary (D). The prediction during Mode B shedding is much better and shows only a small spanwise variation. These observations are borne out when n planes are averaged as shown in Figs. 21 and 24. The predictions are reasonably good for Mode A shedding when four or more planes are used ($n \geqslant 4$). The predictions for Mode B shedding are already good and do not benefit significantly from averaging.

The mean lift coefficient is presented in Fig. 18. Although there is some variation across the span, the values are small and the prediction is generally good. Averaging n planes, as shown in Fig. 22 further improves these predictions.

The standard deviation of the drag coefficient is generally over predicted with this technique as shown in Fig. 20. Although the smallest perimeter ($D = 1.1$) gives a reasonably accurate prediction, the over-prediction significantly increases with larger values of D. Averaging n planes, as in Fig. 24, does not improve the predictions because the standard deviation is over predicted across the span.
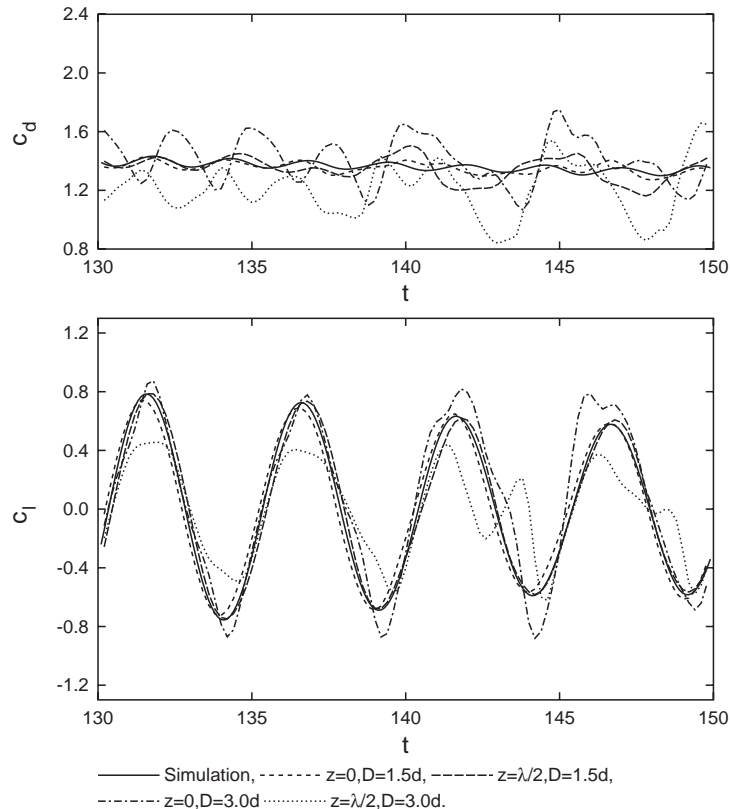
Fig. 15. Time histories of the estimated drag and lift coefficient for Mode A shedding at Re = 260.

4. Conclusions

This study is ultimately focused on the possibility of using experimentally determined velocity data, gathered from PIV measurements, to determine the force acting on a bluff body. The seemingly paradoxical choice of using numerically simulated velocity fields has the advantage of effectively eliminating the influence of noise on the investigation and thus provides an upper limit to the accuracy achievable using this approach. Note that Noca et al. (1999) have shown that PIV data can be used to accurately determine the force on the body if experimental velocity data are used over the entire integration contour.

In the 2-D study, obviously the predictions generally improve when the simulated flow velocity is used on a larger portion of the wake and overall perimeter. The velocity field far from the cylinder is required to accurately predict the mean drag force. This is in contrast to statistical quantities associated with the fluctuations such as standard deviations of the lift and drag force, and the relative phasing of the force signal. Generally, predictions improve as the integration boundary approaches the cylinder. In addition, to obtain a good estimate of the time-dependent lift force probably requires upstream velocity data, or at least data toward the sides of the body. This makes sense because the drag should be mainly influenced by fluctuations at the rear and the lift influenced by fluctuations at the sides. These conclusions are probably a little pessimistic because the potential flow is a better approximation at higher Reynolds numbers. This would likely benefit the mean drag force predictions.

The 3-D study used 2-D projections of the velocity field data over the entire integration contour. The variations of the predictions at different spanwise locations (z) and integration contours (D) at different distances were determined. Predictions made with smaller integration perimeters (D) are generally better and are less sensitive to the spanwise location (z) of the integration contour. This is due to the flow near the cylinder being more 2-D. The predicted mean drag and fluctuating lift force when Mode A shedding dominates is strongly dependent on the spanwise position, especially for larger perimeters (D). This is a result of the large distortion of the 2-D rollers by the Mode A instability. Averaging four of more planes ($n \geqslant 4$) will eliminate the spanwise variation and produce a good estimate. The
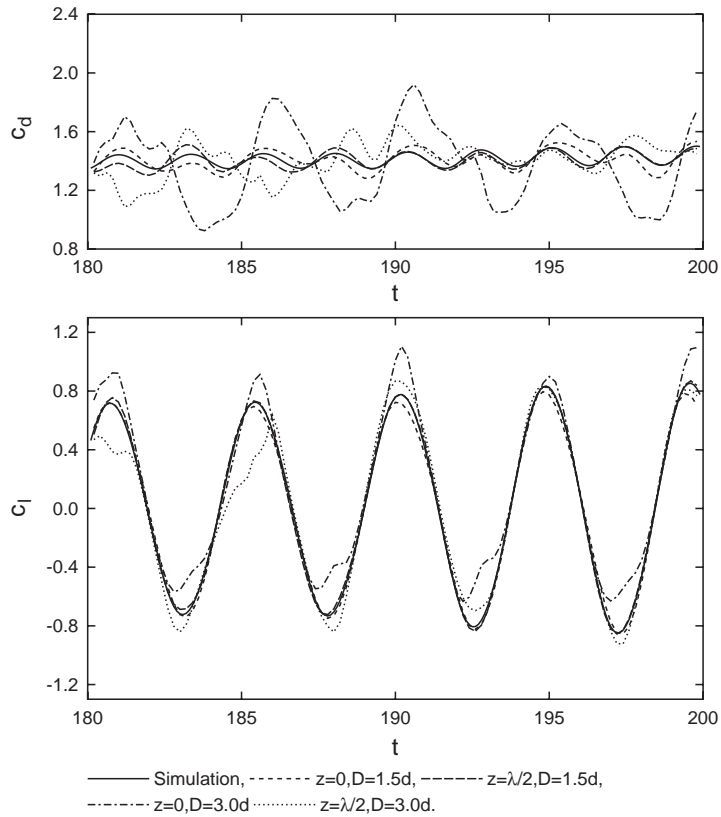
Fig. 16. Time histories of estimated drag and lift coefficients for Mode B shedding at Re = 260.
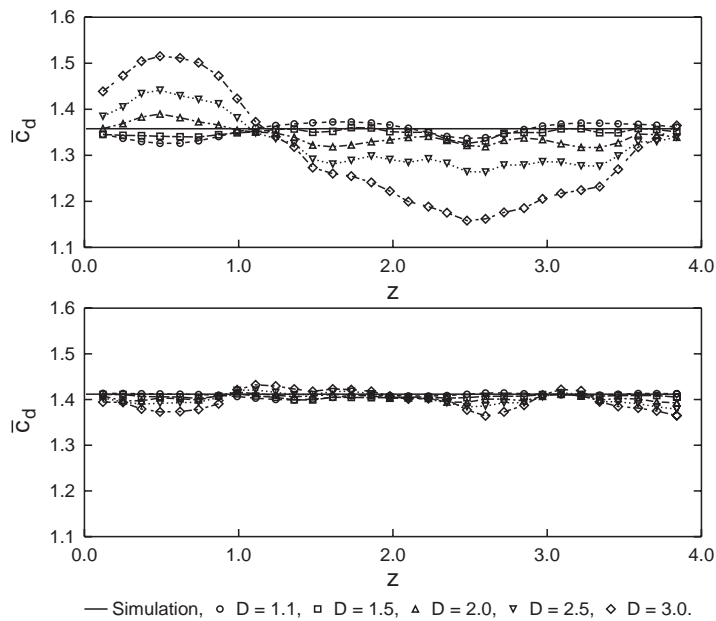

Fig. 17. Prediction of mean drag coefficient as a function of z for the various values of D compared with the simulated value (solid line) for Mode A (top) and Mode B (bottom) shedding.
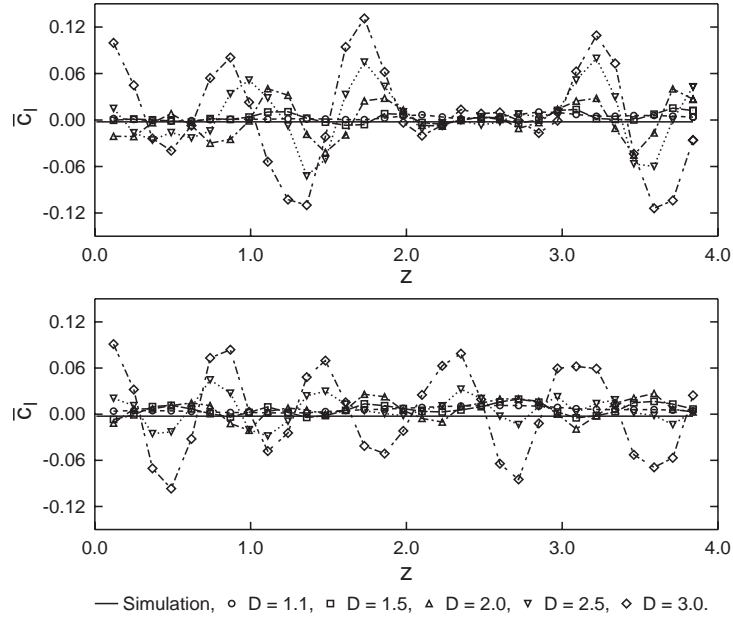
Fig. 18. Prediction of mean lift coefficient as a function of z for the various values of D compared with the simulated value (solid line) for Mode A (top) and Mode B (bottom) shedding.
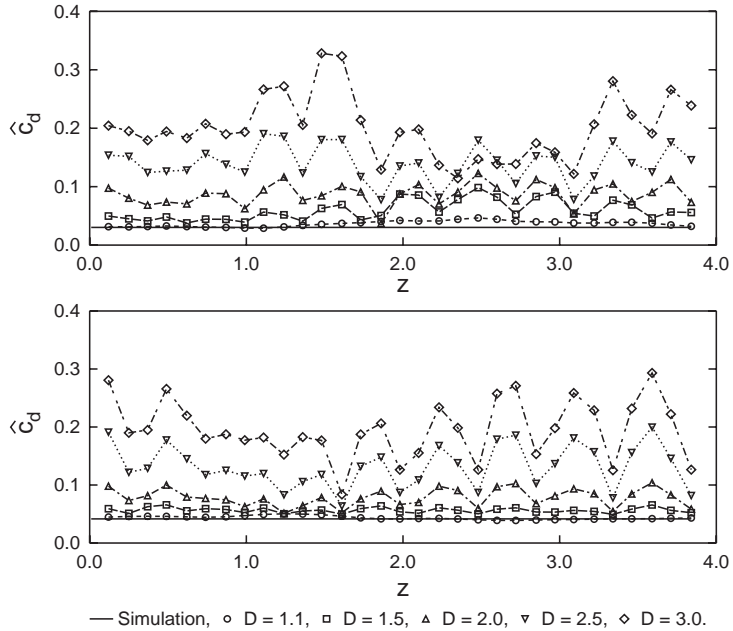

Fig. 19. Prediction of the standard deviation of the drag coefficient as a function of z for the various values of D compared with the simulated value (solid line) for Mode A (top) and Mode B (bottom) shedding.

predictions of mean drag and fluctuating lift force are generally accurate for Mode B shedding and do not significantly benefit from averaging. The mean lift force is well predicted for both shedding modes and the relative difference between the prediction and the simulated force never exceeds 4% of the fluctuating component. Therefore, averaging n planes only shows marginal improvements. The fluctuating lift force is significantly over-predicted, especially for larger values of integration perimeters (D). Averaging across planes does not improve predictions significantly.
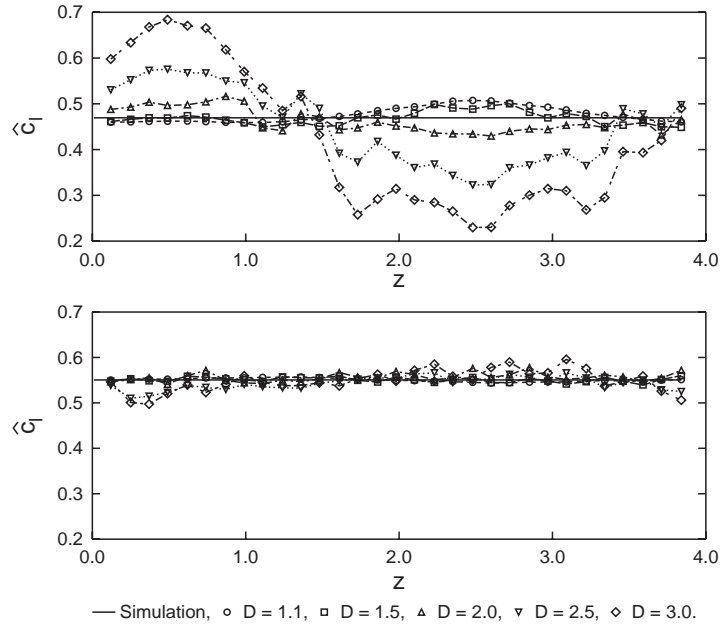
Fig. 20. Prediction of the standard deviation of the lift coefficient as a function of z for the various values of D compared with the simulated value (solid line) for Mode A (top) and Mode B (bottom) shedding.
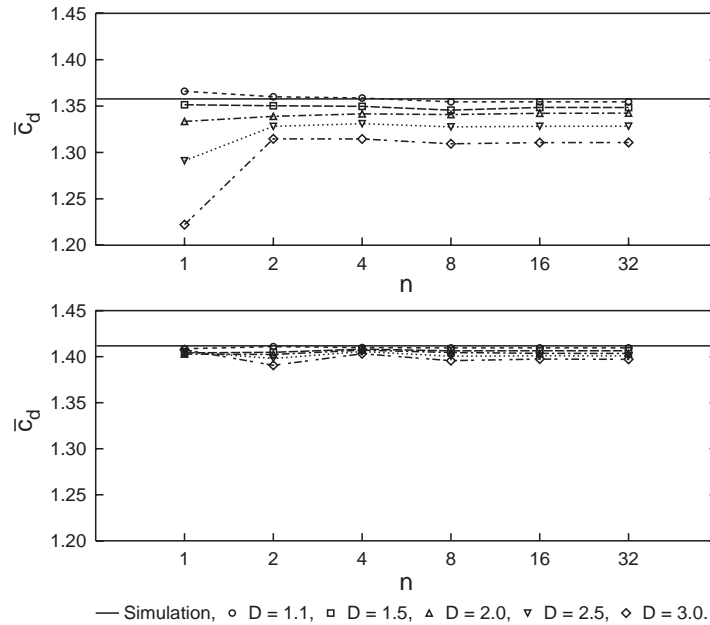

Fig. 21. Prediction of mean drag coefficient averaged across n equispaced planes for the various values of D compared with the simulated value (solid line) for Mode A (top) and Mode B (bottom) shedding.

The general conclusion is that the approach of evaluating forces can be successfully applied for integration contours close to the body. This is preferably when using PIV anyway since the interrogation window is generally small and can usually be positioned to encompass the body. Most importantly, the method avoids the necessity of using PIV data at the boundary of the body where, for the combination of reasons discussed previously, the errors tend to be larger.
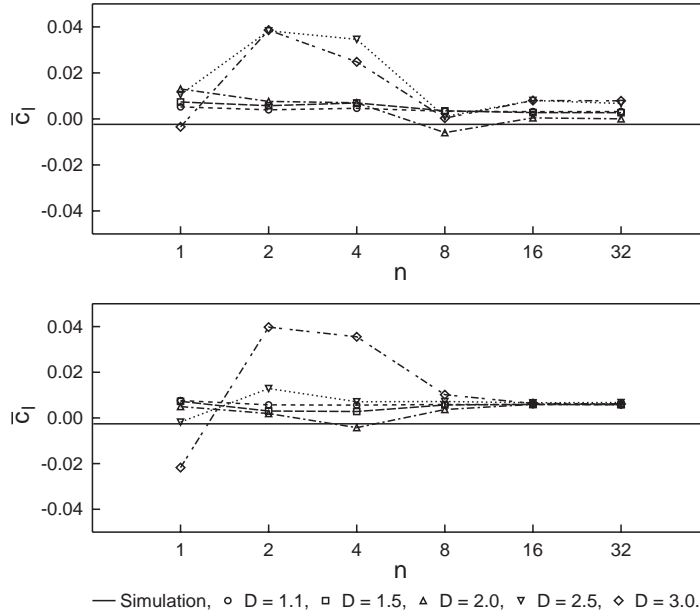
Fig. 22. Prediction of mean lift coefficient averaged across n equispaced planes for the various values of D compared with the simulated value (solid line) for Mode A (top) and Mode B (bottom) shedding.
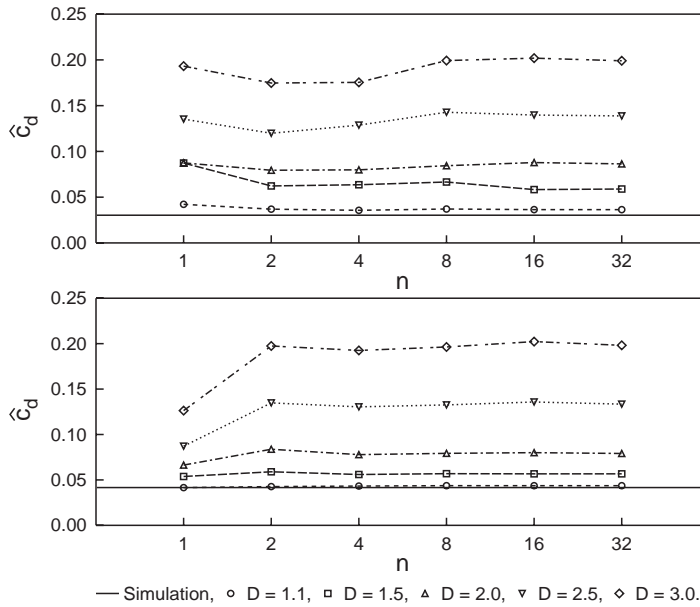
Fig. 23. Prediction of the standard deviation of the drag coefficient averaged across n equispaced planes for the various values of D compared with the simulated value (solid line) for Mode A (top) and Mode B (bottom) shedding.

Acknowledgements

Fig. 24. Prediction of the standard deviation of the lift coefficient averaged across n equispaced planes for the various values of D compared with the simulated value (solid line) for Mode A (top) and Mode B (bottom) shedding.
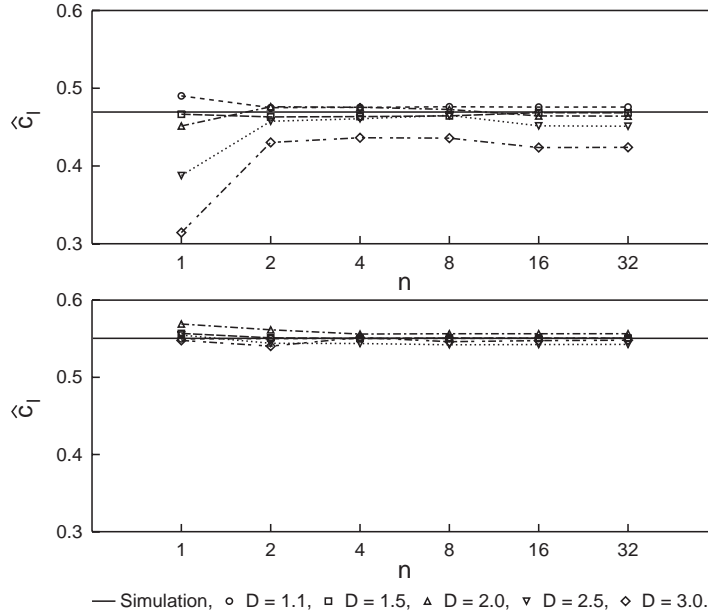
Appendix A. Modified "flux equation" for a periodic flow problem

This section outlines the method used to obtain the modified flux equation. The modified equation is necessary when the bluff body intersects the outer boundary of integration. Firstly, we start with the force balance equation obtained from the control volume analysis as shown by Noca et al. (1999) and reproduced here.

$$\mathbf{F} = -\frac{\mathrm{d}}{\mathrm{d}t}\int_{V(t)} \mathbf{u}\,\mathrm{d}V + \int_{S(t)} \hat{\mathbf{n}}\cdot[-p\mathbf{I}-(\mathbf{u}-\mathbf{u}_s)\mathbf{u}+\mathbf{T}]\,\mathrm{d}S - \int_{S_b(t)} \hat{\mathbf{n}}\cdot(\mathbf{u}-\mathbf{u}_s)\mathbf{u}\,\mathrm{d}S. \tag{5}$$

The 'flux' equation involves only surface integration of velocity data and its derivatives. Two terms need to be rewritten to obtain the 'flux' equations from the above equation. The first term is the time rate of change of the volume integral of velocity. This is rewritten with the aid of (i) a vector identity, (ii) assuming the velocity is divergence free and (iii) Green's Theorem. The procedure is shown briefly below.

$$\begin{aligned}
-\frac{\mathrm{d}}{\mathrm{d}t}\int_{V(t)} \mathbf{u}\,\mathrm{d}V &= -\frac{\mathrm{d}}{\mathrm{d}t}\int_{V(t)} \nabla\cdot(\mathbf{u}\mathbf{x})-(\nabla\cdot\mathbf{u})\mathbf{x}\,\mathrm{d}V \\
&= -\frac{\mathrm{d}}{\mathrm{d}t}\int_{V(t)} \nabla\cdot(\mathbf{u}\mathbf{x})\,\mathrm{d}V, \quad \text{because } \nabla\cdot\mathbf{u}=0 \\
&= -\frac{\mathrm{d}}{\mathrm{d}t}\int_{S(t)+S_b(t)} \mathbf{n}\cdot\mathbf{u}\mathbf{x}\,\mathrm{d}S \\
&= -\int_{S(t)} \mathbf{n}\cdot\frac{\mathrm{d}\mathbf{u}}{\mathrm{d}t}\mathbf{x}\,\mathrm{d}S - \int_{S(t)} \mathbf{n}\cdot\mathbf{u}\mathbf{u}_s\,\mathrm{d}S - \int_{S_b(t)} \mathbf{n}\cdot\frac{\mathrm{d}\mathbf{u}}{\mathrm{d}t}\mathbf{x}\,\mathrm{d}S.
\end{aligned} \tag{6}$$

This derivation is in line with Noca et al. (1999). The only difference is that the inner and outer surfaces are no longer closed but join up to form the boundaries of integration. In this case, Green's theorem is still applicable because the volume of fluid is bounded by the inner surface coinciding with the cylinder surface, the outer cylindrical tube and the circular disk at the periodic boundaries.

The next term that needs to be rewritten is the one involving pressure. The pressure term is removed by assuming the flow obeys the Navier–Stokes (momentum) equations.

$$\nabla p = -\frac{\partial \mathbf{u}}{\partial t} - \mathbf{u}\cdot\nabla\mathbf{u} + \nabla\mathbf{T}. \tag{7}$$

The force balance eq. (5) would contain a double quadrature if the pressure term is replaced by the above eq. (7). Noca et al. (1999) avoids the double quadrature by using Stokes theorem. This is not applicable in this case because the outer surface is not closed when the cylinder intersects this surface. Without using Stoke's theorem, the pressure integral is as follows:

$$\int_{S(t)} \hat{\mathbf{n}} \cdot -p\mathbf{I}\,\mathrm{d}S = \int_{S(t)} \int_{\mathbf{x_o}}^{\mathbf{x}} \hat{I} \cdot \left(\frac{\partial \mathbf{u}}{\partial t} + \mathbf{u} \cdot \nabla \mathbf{u} - \nabla \mathbf{T} \right) \mathrm{d}l\,\mathrm{d}S. \tag{8}$$

When Eqs. (6) and (8) are inserted into the force balance equation (5), the result is a modified "flux" equation, Eq. (4). Note that the surface integrals are no longer closed integrals because both the inner and outer surfaces are no longer closed but instead join up to form a closed surface.

References

Adrian, R.J., 1991. Particle-imaging techniques for experimental fluid mechanics. Annual Review of Fluid Mechanics 23, 261–304.

Albarede, P., Provansal, M., 1995. Quasi-periodic cylinder wakes and the Ginzburg–Landau model. Journal of Fluid Mechanics 291, 191–222.

Barkley, D., Henderson, R.D., 1996. Three-dimensional Floquet stability analysis of the wake of a circular cylinder. Journal of Fluid Mechanics 322, 215–241.

Dusek, J., Le Gal, P., Fraunie, P., 1994. A numerical and theoretical study of the first Hopf bifurcation in a cylinder wake. Journal of Fluid Mechanics 264, 59–80.

Etoh, G.T., Takehara, K., Takano, Y., 2002. Development of high-speed video cameras for dynamic PIV. Journal of Visualization 5 (3), 213–224.

Heineck, J.T., Schultz, P.H., Anderson, J.L.B., 2002. Application of three-component PIV to the measurement of hypervelocity impact ejecta. Journal of Visualization 5 (3), 233–242.

Henderson, R.D., 1997. Nonlinear dynamics and pattern formation in turbulent wake transition. Journal of Fluid Mechanics 352, 65–112.

Hinsch, K.D., 2002. Holographic particle image velocimetry. Measurement Science and Technology 13 (7), R61–R72.

Hourigan, K., Thompson, M.C., Tan, B.T., 2001. Self-sustained oscillations in flows around long blunt plates. Journal of Fluids and Structures 15 (3/4), 387–398.

Karniadakis, G.E., Israeli, M., Orszag, S.A., 1991. High-order splitting methods for the incompressible Navier–Stokes equations. Journal of Computational Physics 97, 414–443.

Konrath, R., Schrvder, W., Limberg, W., 2002. Holographic particle image velocimetry applied to the flow within the cylinder of a four-valve internal combustion engine. Experiments in Fluids 33 (2), 781–793.

Lin, J.-C., Rockwell, D., 1996. Force identification by vorticity fields: techniques based on flow imaging. Journal of Fluids and Structures 10 (6), 663–668.

Meyer, K.E., Vzcan, O., Westergaard, C.H., 2002. Flow mapping of a jet in crossflow with stereoscopic PIV. Journal of Visualization 5 (3), 225–232.

Noca, F., Shields, D., Jeon, D., 1999. A comparison of methods for evaluating time-dependent fluid dynamics forces on bodies, using only velocity fields and their derivatives. Journal of Fluids and Structures 13 (5), 551–578.

Scarano, F., van Wijk, C., Veldhuis, L., 2002. Traversing field of view and AR-PIV for mid-field wake vortex investigation in a towing tank. Experiments in Fluids 32 (1), 950–961.

Tan, B.T., Thompson, M.C., Hourigan, K., 1998. Flow around long Rectangular Plates under Cross-flow Perturbations. International Journal of Fluid Dynamics (http://elecpress.monash.edu.au/IJFD), 2, Article 1.

Thompson, M.C., Hourigan, K., Sheridan, J., 1996. Three-dimensional instabilities in the wake of a circular cylinder. Experimental Thermal and Fluid Science 12 (2), 190–196.

Unal, M.F., Lin, J.-C., Rockwell, D., 1997. Force prediction by PIV imaging: a momentum-based approach. Journal of Fluids and Structures 11 (8), 965–971.

Upatnieks, A., Laberteaux, K.L., Ceccio, S.L., 2002. A kilohertz frame rate cinemagraphic PIV system for laboratory-scale turbulent and unsteady flows. Experiments in Fluids 32 (1), 87–98.

Williamson, C.H.K., 1996. Three-dimensional Wake Transition. Journal of Fluid Mechanics 328, 345–407.

Williamson, C.H.K., 1988. The existence of two stages in the transition to 3-Dity of a cylinder wake. Physics of Fluids 31 (11), 3165–3168.

Williamson, C.H.K., Roshko, A., 1988. Vortex formation in the wake of an oscillating cylinder. Journal of Fluids and Structure 2, 355–381.

Wu, J., Sheridan, J., Welsh, M.C., Hourigan, K., 1996. Three-dimensional vortex structures in a cylinder wake. Journal of Fluid Mechanics 312, 201–222.